Complex nanoemulsion for vitamin delivery

Machado, Neila; Bruininks, Bart M H; Singh, Priyanka; Dos Santos, Laurita; Dal Pizzol, Carine; Dieamant, Gustavo de C; Kruger, Odivania; Martin, Airton A; Marrink, Siewert J; Souza, Paulo C T

Published in:
Nanoscale

DOI:
10.1039/d1nr04610a

Publication date:
2022

Nanoscale

PAPER

View Article Online
View Journal

Cite this: DOI: 10.1039/d1nr04610a

Complex nanoemulsion for vitamin delivery: droplet organization and interaction with skin membranes†

Neila Machado, *[a,b] Bart M. H. Bruininks, ‡[c] Priyanka Singh,‡[a] Laurita dos Santos, [a,d] Carine Dal Pizzol,[e] Gustavo de C. Dieamant,[e] Odivania Kruger,[e] Airton A. Martin, [d,f] Siewert J. Marrink, [c] Paulo C. T. Souza *[c,g] and Priscila P. Favero *[d]

Lipid nanoemulsions are promising nanomaterials for drug delivery applications in food, pharmaceutical and cosmetic industries. Despite the noteworthy commercial interest, little is known about their supramolecular organization, especially about how such multicomponent formulations interact with cell membranes. In the present work, coarse-grained molecular dynamics simulations have been employed to study the self-assembly of a 15-component lipid nanoemulsion droplet containing vitamins A and E for skin delivery. Our results display aspects of the unique "onion-like" agglomeration between the chemical constituents in the different layers of the lipid nanodroplet. Vitamin E molecules are more concentrated in the center of the droplet together with other hydrophobic constituents such as the triglycerides with long tails. On the other hand, vitamin A occupies an intermediate layer between the core and the co-emulsifier surface of the nanodroplet, together with lecithin phospholipids. Coarse-grained molecular dynamics simulations were also performed to provide insight into the first steps involved in absorption and penetration of the nanodroplet through skin membrane models, representing an intracellular (hair follicle infundibulum) and intercellular pathway (stratum corneum) through the skin. Our data provide a first view on the complex organization of commercial nanoemulsion and its interaction with skin membranes. We expect our results to open the way towards the rational design of such nanomaterials.

Received 15th July 2021,
Accepted 6th November 2021

DOI: 10.1039/d1nr04610a

rsc.li/nanoscale

1 Introduction

A nanoemulsion is a colloidal particle system with a droplet size in the range of 20 to 500 nm. Immiscible liquids are mixed to form a liquid-in-liquid dispersion, by means of an emulsifying agent like surfactants and co-surfactants.[1–3] These kinetically stable systems appear to be promising for efficient delivery of active molecules. The range of nanoemulsion applications spans diverse fields including drug delivery, as formulations for transdermal delivery of celecoxib;[4] the food industry, where bioaccessibility of long chain triglyceride nanoemulsions with β-carotene have been investigated;[5] and in the cosmetic industry where nanoemulsions have been tested for skin hydration and ease of application.[6,7] The main advantages of nanoemulsions over other drug delivery vectors are their capability to: (i) encapsulate both hydrophilic and hydrophobic molecules; (ii) improve the bioavailability of such molecules; (iii) deliver selectively at a target site; (iv) and finally, they have reduced toxicity.[8,9]

Although a great variety of nanoemulsion formulations have been synthetized and tested, only limited high-resolution data exist regarding supramolecular organization of such materials. Relevant efforts have been made using a multitude of experimental techniques (*e.g.* solid-state NMR, AFM) to investigate, for instance: nanoparticle self-assembly from amphiphilic peptides;[10] complexes of cationic lipids and oligo-

[a]Institute of Research and Development, Universidade do Vale do Paraíba, Av. Shishima Hifumi 2911, 12244-000, São José dos Campos, São Paulo, Brazil
[b]UFABC Universidade Federal do ABC, Avenida dos Estados, 5001, 09210-580, Santo André, São Paulo, Brazil. E-mail: neilamachado@gmail.com
[c]Groningen Biomolecular Sciences and Biotechnology Institute and Zernike Institute for Advanced Materials, University of Groningen, Nijenborgh 7, 9747 AG Groningen, The Netherlands
[d]Biomedical Engineering Innovation Center, Biomedical Vibrational Spectroscopy Group. Universidade Brasil UnBr, Rua Carolina Fonseca 235, 08230-030, Itaquera, São Paulo, Brazil. E-mail: priscila.favero@universidadebrasil.edu.br
[e]Grupo Boticário, Av. Rui Barbosa, 4110, 83055-010, Parque da Fonte, São José dos Pinhais, Paraná, Brazil
[f]DermoProbes – Research, Innovation and Technological Development, Av. Cassiano Ricardo, 601, Sala 73-74, 12246-870, São José dos Campos, SP, Brazil
[g]Molecular Microbiology and Structural Biochemistry (MMSB, UMR 5086), CNRS, University of Lyon, Lyon, France. E-mail: paulocts@gmail.com

†Electronic supplementary information (ESI) available. See DOI: 10.1039/d1nr04610a

‡Authors contributed equally.

nucleotides;[11] and direct and reverse nanodroplets of water, oil and dioctyl sodium sulfosuccinate[12] as well as the interactions of such nanodroplet with membranes. However, the inherently small size of nanodroplets and the often short life times of transition states makes simulation an important complementary approach to experiment.[13,14] All-atom (AA) and coarse-grained (CG) molecular dynamics (MD) simulations have been used for studies of simple binary and ternary mixtures, representative of nanoemulsion formulations,[15–18] and have steadily increased in complexity and scale.

Computational and experimental studies involving the interaction of nanocapsules with lipid bilayers have been performed in the last years.[19–22] From a more general perspective, simulation methods have been extensively applied in the nano-bio interface, as a way to support and interpret the experimental results.[22,23] For instance, computational studies with model systems have been performed to understand the effect of nanocapsule sizes, shapes, charge, elasticity, hydrophobicity and coating in the interactions with lipid membranes.[23–30] Even the more realistic models usually only involve hard solid-like nanoparticles, including the ones composed of fullerenes[31,32] or gold coated nanoparticles with polymers or surfactants.[33–37] The wrapping process of softer delivered systems is less understood, but there are some examples in the literature as well. For instance, dendrimer nanoparticles interactions with membrane models have been investigated using dissipative particle dynamics,[38] while CG simulations were used to study the fusion of perfluorocarbon-based nanodroplets with phospholipid vesicles.[39] Except for recent efforts, including lipoplexes[40,41] and Gelucire 50/13 lipid nanoparticles,[42] most of the computational studies used rather simple bilayer models, and they were focused on understanding how the nanoparticle can penetrate or change the bilayer properties.[43] Recently, much effort has been devoted to model more complex membranes, including skin membranes,[44–46] which open the possibility to simulate the uptake of nanodroplets more realistically.

In the current work, we performed CG MD simulations to study the complex organization of nanodroplets from a commercial nanoemulsion formulation. Such nanoemulsions are used as a cosmetic for the delivery of hydrophobic vitamins A and E through the skin. We show that a nanodroplet of given composition presents an onion-like organization, with vitamins A and E differently distributed in different layers of the droplet. Besides, we investigate the onset of the fusion of the multicomponent nanodroplet with two complex bilayer models, mimicking the hair follicle (infundibulum, INF) and stratum corneum (SC) of human skin. To do so, we utilized the CG Martini force field as it provides a wide range of compatible molecules allowing for simulation of complex mixtures, with only limited additional parametrization.[47,48] Another important aspect of CG is that the potentials are smoother and the simulations contain less particles, offering a 2–3 order of magnitude speedup compared to AA models. This allows for equilibrating the structural organization of the multicomponent nanodroplets near to their realistic sizes, and to simulate the initial stages of the fusion of the nanodroplet with skin membranes. The spatial and time scales explored here are inaccessible for the current experimental techniques typically used to study nanoemulsion and their interactions with skin.[3] So, our main aim was to provide an molecular picture of complex nanoemulsion formulations and their possible transdermal delivery mechanisms.

2 Methods

2.1 Building the lipid nanodroplet model

The chemical composition of the lipid nanoemulsion was provided by Boticário company, which is involved in the production and marketing of this formulation. A complete overview of the composition can be found in Table 1. The molar percentage of components of the same type were equally distributed.

The major carrier components of the formulation are triglycerides, which are often used as carriers of fat-soluble vitamins and other bioactives. The ST21 (polymer-based polyethylene glycol with a 16C acyl terminal) is added to enhance emulsion stability. It is important to note that the nanodroplet has zero net charge and no negatively charged molecules. Palmitic and stearic acids were considered in their protonated (neutral) state.

In order to produce the lipid nanodroplet model for the nanoemulsion, we first assembled the hydrophobic compounds. Then we added the amphiphilic constituents to form the final nanodroplet. These stages correspond to the experimental process of forming the lipid nanoemulsion (personal communication).[49] In the first phase, vitamins A and E were mixed with triglycerides (capric and caprylic). The remaining excipients were added in phase two. For the first stage of lipid nanoemulsion formation, we used a box of $26 \times 26 \times 26$ nm^3 with 123 938 CG water beads (corresponding to 495 752 water

Table 1 Components of the lipid nanoemulsion by type and molar percentage. The name of the components follows the INCI nomenclature for cosmetic ingredients

Component	Abbreviation	Type	Molar percentage %
Retinol	VITA	Vitamin A	20.06
Tocopherol	VITE	Vitamin E	20.03
Caprylic/capric triglyceride	CPLC/CPRC	Triglyceride	28.79
Cetyl palmitate	CPAL	Lipid	7.21
Glyceryl stearate	GLST		
Cetyl alcohol	CAL		
Lauryl alcohol	LAAL		
Behenyl alcohol	BHAL	Blend lipids	4.27
Myristyl alcohol	MYAL		
Palmitic acid	PALAC		
Stearic acid	STAC		
Glycerin	GLC	Humectant	4.80
Hydrogenated lecithin 90G	HLEC	Phospholipid	4.80
Lecithin 80H	LEC	Phospholipid	3.02
Steareth-21	ST21	Co-emulsifier	7.02

molecules). After 1000 steps of minimization, stage 1 was equilibrated for 400 ns at an elevated temperature of 353 K to speed up the equilibration. In the second stage, we also used box of 26 × 26 × 26 nm^3, but with slightly less water, with 103 193 CG water beads. The equilibration of stage 2 covered 1000 ns. A final step was performed for additional 1000 ns to equilibrate the nanodroplet at 310 K. In all steps, the pressure was controlled with an isotropic coupling scheme. The size of the nanodroplet was controlled by the total number of components added to simulation boxes. The choice of nanodroplet size used (around 20 nm) was based on a compromise between representing a realistic diameter and computational cost for the simulations.

2.2 Building the skin bilayer models

The biochemical composition of the skin is strongly dependent on both extrinsic and intrinsic factors (such as sun exposure, diet, and daily habits; chronological aging),[50–52] thus, the models that we intend to use to mimic the composition of the skin must contain information that particularizes the case to be studied. Our studies were based on the construction of skin models of healthy people.[53] Fig. S1 and S2† illustrate the INF and SC membranes and the possible permeation pathways in which the nanodroplet interacts with the respective membrane. Bilayer compositions are based on Machado *et al.* 2016.[54] The INF bilayer includes 14 different types of compounds, among them cholesterol, ceramide, sphingomyelins and various types of phospholipids. This membrane shows similar characteristics to the plasma membrane model of Ingólfsson *et al.* 2014.[55] The SC was composed of a mixture of ceramides, cholesterol and fatty acids. As low pH conditions could be important for the permeability and phase state of SC bilayers,[56,57] we built two models in this case: neutral (low pH, with fatty acids fully protonated) and charged (neutral pH, with fatty acids deprotonated). All simulation boxes were built with insane·py,[48] with the bilayers placed in a box of around 35 × 35 × 35 nm^3 in size, which was solvated with ~300 000 CG water beads and 0.15 M of NaCl. After 1000 steps of minimization, the systems were equilibrated at 310 K for 1000 ns. Pressure was controlled semi-isotropically. The temperatures of the membrane, and the solvent were maintained separately at 310 K.

2.3 Fusion simulations

The equilibrated nanodroplet and membranes generated in the previous steps were used as initial conditions for the fusion simulations. We placed the nanodroplet on top of each bilayer at around 9.7 nm distance between their centers of geometry. At this distance, the nanodroplet starts with one to two water solvent shells between its surface and the bilayer headgroups. The standard sized fusion experiments (43 × 43 × 29 nm^3) contained ~33 450 CG water beads and 0.15 M NaCl. Production simulations were performed at 310 K and 1 bar during at least 1000 ns. In the case of INF bilayers, a box with lateral dimensions four times larger was also tested.

2.4 CG models

The Martini force field was used for all CG simulations.[47,58] Concerning the nanodroplet, topologies of standard lipids were taken from the work of Wassenaar *et al.* 2015.[48] Topologies for a number of less standard components were optimized to improve their mapping and water–octanol partitioning, including capric and caprilic triglycerides, hydrogenated lecithin cetyl palmitate, glyceryl stearate, cetyl alcohol, lauryl alcohol, behenyl alcohol, myristyl alcohol, palmitic acid, stearic acid, the mapping for these molecules can be found in Table S1.† The topology for the co-emulsifier Steareth 21 was based on the work of Rossi G. *et al.* 2012.[59] Vitamin A (retinol), vitamin E (tocopherol) and humectant (glycerin) were parameterized following the standard procedure as described by Marrink *et al.*[47,58,59] For the non-bonded parameters, the water–octanol partitioning free energy of the CG model was compared to the experimental value for each molecule (Table S2†). To calculate these free energies of transfer we used the same methodology as was used in ref. 60. For the bonded parameters, the suggested default values were used (Table S3†). For the skin bilayer lipids, the current Martini models were used.[47,48,61] Although the current models of vitamins may suffer from some pitfalls of Martini 2,[60] we do not think that new version of Martini force field[62] would qualitatively change the results presented here, as Martini 2 has consistently shown reasonably accuracy in simulations of lipids and complex biomembranes.[63]

2.5 Simulation parameters

All simulations were performed using GROMACS 5.x/2016.[64–68] The parameters were accordingly taken from the Martini default settings.[69] Each CG production run was preceded by an initial energy minimization of the system using the steepest descent algorithm. The integrator used for equilibration and production runs was the leap-frog algorithm,[70] with an integration time step of 20 fs. Neighbour searching was calculated using the Verlet scheme[71] at a 20 step interval. Electrostatic interactions were calculated using the Reaction-Field algorithm with a dielectric constant of 15. The cut-off for van der Waals and electrostatic interactions were set at 1.1 nm, furthermore, the van der Waals and Coulombic interactions were shifted between 0.9–1.1 and 0.0–1.1 nm respectively using Potential-shift-Verlet. Temperature was set using V-rescale,[72,73] with each phase coupled separately to the thermostat with a coupling time constant of 1.0 ps. Pressure control was performed with the Parrinello-Rahman barostat[74] with a reference pressure of 1 bar, a coupling time constant of 12 ps and an isothermal compressibility of 3×10^{-4} bar^{-1}. The pressure coupling was set to semi-isotropic and isotropic for systems with and without a bilayer respectively, unless specifically stated otherwise. Cuboid periodic boundary conditions were used in all cases.

2.6 Analysis of the skin membranes models

The skin membrane models were characterized based on the order parameter. The order parameter was calculated on the last 100 ns of a 1 μs spanning production simulation of the

respective bilayer (infundibulum, stratum corneum with and without charged fatty acids). Making use of MDAnalysis,[75,76] Numpy,[77] Freud,[78] Matpotlib[79] and Lipyphillic,[80] we calculated the order parameter of all lipid tails in the membranes and projected it on the lipid linkers (GL1 and GL2 beads), as defined in the Lipyphilic[80] order parameter tutorial. The order parameter algorithm for coarse grained systems was first published in the work of Seo *et al.* 2020.[81] This procedure was designed to work well for relatively flat bilayers.

2.7 Analysis of nanodroplet and fusion simulations

The radius of gyration (R_g) was used as a simple metric to verify the equilibration of the assembled nanodroplet in both stages. R_g over time of the nanodroplet was determined using the default GROMACS 2016 gmx gyrate tool. The solvent accessible surface area (SASA) was used to estimate the diameter of the assembled nanodroplet (in both stages). SASA has been computed using the GROMACS 2016 gmx sasa tool, with 400 grid points and a 1.00 nm probe. The nanodroplet was approximated to a perfect sphere, with its surface area (SA) approximated to be SA = $4\pi r^2$ = SASA. The diameter (d) was obtained with the radius (r), which was shifted considering the size of the probe – $d = 2 \times (r - r_{probe})$.

Besides looking at the nanodroplet as a whole we used the radial distribution function (RDF) to study the spherical organization of the individual components and their internal chemical groups with respect to the center of mass of the nanodroplet. The RDF was calculated using the GROMACS rdf tool. The chemical groups were specified based on their CG bead types, separating the hydrophobic (tails; C type) and hydrophilic regions (heads, linkers; N, P, Q types).

Mixing of components during fusion was analyzed using a custom VMD script written partially in TCL and python3. First we determined the distances of all components with respect to all the other components (taking into account periodic boundary conditions). All query molecules within 0.8 nm of a target molecule were considered in contact. Molecules could have multiple contacts between them by this definition. As position of the minimum in the Lennard-Jones potential of Martini 2 regular beads is 0.53 nm, a cutoff of 0.8 nm was considered a reasonable choice, as it would include beads in slightly longer distances, given the thermal fluctuation. The contacts were split into two groups: nanodroplet and bilayer. Contacts within one group were normalized by the initial contacts value, where contacts between the droplet and the bilayer were normalized based on their final amount of contacts. The contacts were calculated for the first 1000 ns of the fusion process.

Visual inspection and image rendering was performed using VMD[82] and graphs were generated using XMGRACE and the python3 [83] matplotlib library.[84]

3. Results

3.1 Assembling the nanodroplet

The nanodroplet was assembled in two stages (Fig. 1), which mimics the experimental procedure used to produce the lipid nanoemulsion. In stage 1 (Fig. 1B–D), at an elevated temperature of 350 K, only the vitamins (A/E) and the capric/caprylic acids were added in a dispersed fashion. The components immediately started to aggregate and within 250 ns a spherical assembly was formed with a diameter of 15.2 ± 0.4 nm (Fig. 1D and H). After obtaining stable hydrophobic aggregate, the remaining components of stage 2 (Table 1, excluding the stage 1 components) were added in the same dispersed fashion but quickly start to associate to the stage 1 nanodroplet (Fig. 1E and F). The stage 2 simulation was performed for 1000 ns with R_g indicating a new stable aggregate at 650 ns (Fig. 1I). After the assembly was completed the whole system was cooled down to 310 K, in line with the manufacturing protocol, resulting in a nanodroplet a diameter of with 19.3 ± 0.5 nm (Fig. 1G).

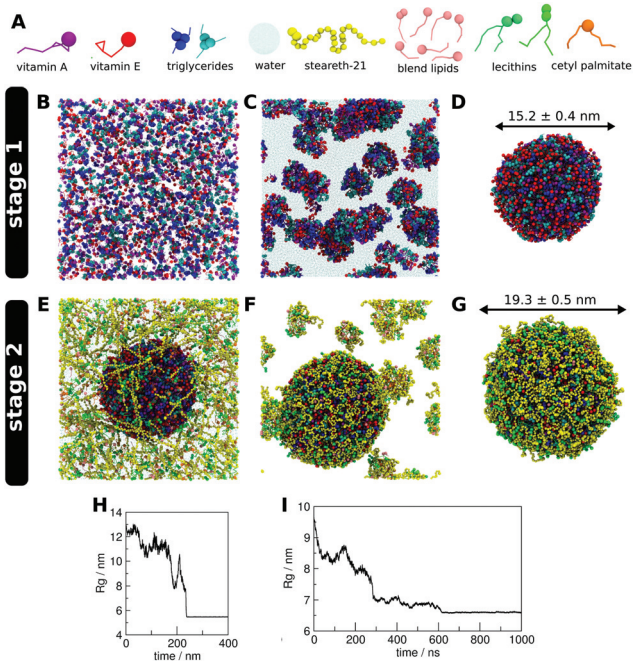

Fig. 1 Stage 1 and 2 of the nanodroplet self-assembly. In (A) is shown the names and color legend of all the nanodroplet components. Snapshots of the self-assembly of components over time for stage 1 (B–D) and stage 2 (E–G) are exemplified. The final snapshot of each stage (D and G for stage 1 and 2, respectively) also indicate an estimate of the nanodroplet diameter (see Methods section for more details). The radius of gyration (R_g) of the nanodroplet was used as metric to verify the equilibration in stage 1 (H) and 2 (I).

3.2 Characterization of the nanodroplet

To obtain a deeper understanding of the structure of the cooled stage 2 complex, we looked at the relative position of all the components (Fig. 2A and B). In addition, we labeled the hydrophilic and hydrophobic parts of the components (Fig. 2C). We reduced the complexity of the figure by splitting the components based on their relative general position separating the core, intermediate and external layer (Fig. 2D, F and H respectively). This splitting was based on the intersections

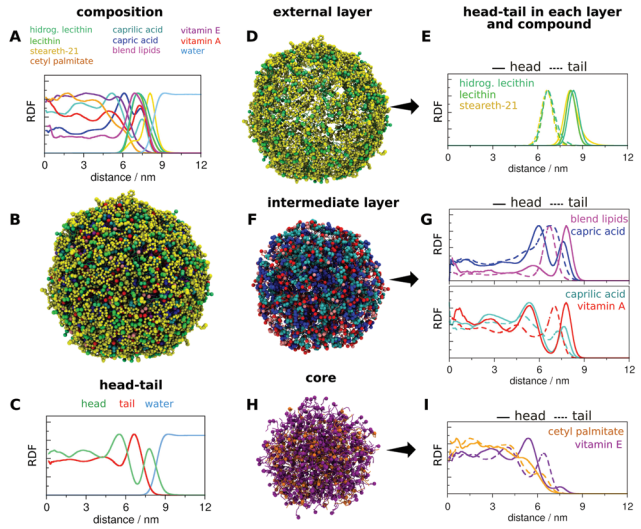

Fig. 2 Nanodroplet structure. (A) The spatial distribution of all components in the nanodroplet, with zero indicating the center of mass. (B) A snapshot of the final nanodroplet. (C) The spatial distribution of the heads and tails as defined by their CG bead type. (D, F and H) Snapshots of the individual layers of the nanodroplet, classified as external (D), intermediate (F) and core (H). (E, G, and I) Distribution of heads and tails for each indicated layer.

of the hydrophilic heads and the hydrophobic tails curves observed in the head–tail graph (Fig. 2E, G and I).

Based on the radial distributions, vitamin E (more hydrophobic than vitamin A) shows to be highly enriched in the inner core together with cetyl palmitate (Fig. 2H and I), whereas vitamin A was distributed both in the core and intermediate layer. The intermediate layer is formed by the phospholipids (in blue), providing support to both the core and the formed layer of vitamin A (in red) and short-tailed triglycerides (Fig. 2F and G). The surface of the nanodroplet was coated by the emulsifier steareth 21, with its hydrophilic polyethylene glycol tail mainly lying on the complex surface and its 16C acyl chain anchored in the outer layer of the nanodroplet. Except for cetyl palmitate, the nanoemulsion components show a strong preferred orientation in the nanodroplet as indicated by the large difference between the solid and dashed curves in the RDF graphs, representing the head and tail parts of the constituents, respectively (Fig. 2E, G and I).

3.3 Fusion with skin membrane models

After obtaining a stable nanodroplet, we constructed two bilayers to model the skin membrane – SC and INF. Both the SC and INF model might be relevant for delivery of active components such as vitamin A/E over the skin barrier. The SC model represents the rather saturated, ordered and rigid membrane of cells in the outer layer of the skin.[54,63] As the real protonation state of the fatty acids is unknown, we created both a protonated and deprotonated version of the SC model to at least cover the extremes. The INF model mimics the membrane conditions inside a hair follicle and is known to be less ordered, more soft and flexible in nature due to its higher unsaturation compared to the SC.[85,86] Equilibrated snapshots for both INF and SC membranes are shown in Fig. S1 and S2.† Order parameters was computed for both membrane models, with the SC model confirmed to be more ordered than INF (Fig. S3–S5†). To simulate fusion, in both models the full nanodroplet was placed in close proximity of the target bilayer (~1 nm). The simulation parameters were chosen such that they mimic biological conditions with respect to salt, pressure and temperature (0.15 M NaCl; 1 bar; and 310 K respectively). All fusion simulations spanned 1 μs and were performed three times except for the large INF system which was only simulated once.

The charged SC fusion experiments ran stable in all cases and no major membrane deformations were observed. Over a period of 1 μs the nanodroplet adsorbed onto the membrane and the exchange of components between the membrane and nanodroplet was visible by eye (Fig. 3A). To quantify this mixing we used the change of molecular contacts over the simulation. From the reduction in nanodroplet self-contacts (Fig. 3C) it is clear that lecithins and some blend lipid species mixed the most. Steareth 21, which is in the outer layer, did mix slightly less than lecithins, which may be a kinetic effect, given the larger mass of this polymeric surfactant. Finally, the components dominantly present in the core show an extremely low change in contacts. From the decay in bilayer self-contacts we conclude that all bilayer components are moving equally fast from the bilayer into the nanodroplet, with very small differences when considering the charged states of the SC model (Fig. 3E). The neutral SC membrane showed a near identical fusion profile, with respect to both the membrane curvature and mixing (Fig. S6†). Details of the system can be found in the ESI.†

In contrast to the SC simulations, the INF membranes showed heavy undulation in our fusion experiments (Fig. 3B). Blend lipids of the nanodroplet, as myristyl and lauric alcohols (MYAL and LAAL, respectively), were the components mixing the most with this skin membrane model (Fig. 3D). In general, these blend lipids mixed around 1.3 times more with INF than the SC models. The rest of the components, which includes the vitamins in the nanodroplet core, shows similar results with SC membrane models, with almost no mixing with the skin membranes. Surprisingly, the decay in INF bilayer self-contacts (Fig. 3F) indicates that cholesterol seems to be the membrane component that diffuses faster to the nanodroplet, with 1.3 to 1.5 times more contacts than all the other components in the INF membrane.

The heavy undulations observed with INF models were also observed in additional fusion simulations with larger membrane models (Fig. S7†). As we observe some unrealistic membrane folding (Fig. S8†), given the periodic boundary conditions, the simulations could not be extended to more than 1 μs, which is a limitation of the approach.

4 Discussion and conclusion

Characterizing the complex molecular organization of nanoemulsions can be fundamental to understand its delivery

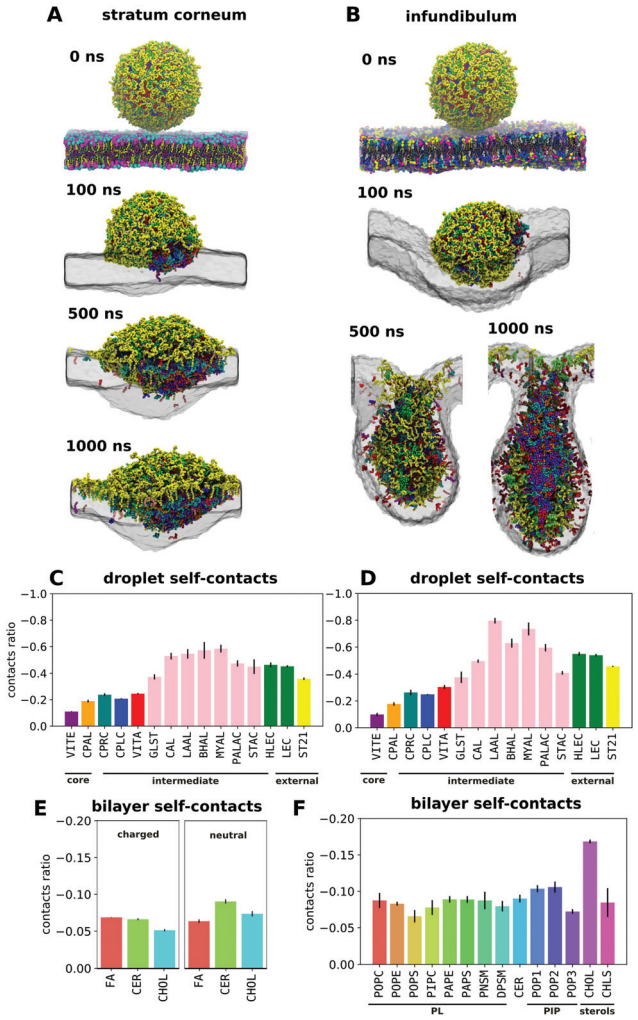

Fig. 3 Nanodroplet fusion with skin membranes. The fusion of the nanodroplet with the stratum corneum (A) and infundibulum (B) membrane models are shown, with some snapshots of unbiased fusion simulations illustrating successive moments in time. The change in self-contacts between the initial 0 ns and final frame 1000 ns are shown with bar plots (C, D, E, and F). They show the change in self-contacts of nanodroplet (C and D) and bilayers (E and F) between the initial (0 ns) and final (1000 ns) frames. The components of the nanodroplet are sorted by the distance of their peak in the RDF from the center of mass of the nanodroplet.

mechanism. However, given the high computational cost to model the macroscopic emulsion, only a representative droplet was considered in this work. Using the same components and procedures described by the nanoemulsion manufacturer, we were able to obtain a stable nanodroplet, which is representative model of the smaller particle sizes expected in the diameter distribution of typical nanoemulsions. The nanodroplet contained a fuzzy-layered onion like internal organization, with the vitamins enriched at its core. Most components showed a strong preferred orientation although the inner core was less ordered than the outer layers.

To obtain a better understanding of the possible delivery of active components, the nanodroplet was placed on different skin membrane models. The main questions considered in this approach were: (i) which skin membrane models is the most favorable for the delivery of vitamins (ii) which is the most probable delivery mechanism: passive mechanisms as diffusion through the membranes or endocytosis of the droplet. Passive diffusion would depend on the mixing and flip-flop of the vitamins in the membrane, which does not seem to be meaningful in our simulations. The results suggested that only little vitamin A/E entered the target in both bilayers model, as the core of nanodroplets tends to stay intact during the simulation time (1 μs). This behaviour is in line with other examples of systems containing high concentration of oils in membranes as triglycerides in lipid droplets[87] and certain hydrophobic polymers added to membranes.[88]

Only the lipids and surfactants in the external and intermediate layer tends to mix with the membranes, with no noticeable flip-flop of the components of the external layer of the nanodroplet to the inner layer of the skin bilayers. On average, the blend lipids of the nanodroplet mixed 30% more with the INF than the SC bilayers (considering both neutral or charged SC models). In addition, the nanodroplet extracted more cholesterol from the INF than SC membranes. Besides the difference in mixing of nanodroplet components between the INF and SC bilayer models, there was a clear difference in membrane undulation. The SC showed little to none bilayer curvature, where the INF showed heavy undulation. Such results suggest that this curvature might induce lipid triggered endocytosis/invagination by the target cells, allowing the nanodroplet components to enter the cell by other means than passive diffusion. Although our simulations show curvature in a random direction, the asymmetry in the plasma membrane has been shown to cause such curvature to bend inwards and can be strongly dependent on cholesterol depletion.[89,90] Other means of endocytosis such as clathrin or caveolin dependent pathways are an option as well for the INF.[91] Therefore it seems likely that more active components would cross over the INF than the SC membrane. However, it is important to consider that the hairsacks only take up roughly 0.1% of the surface of the exposed skin, possibly influencing the delivery efficiency of this path.[92,93] Future experimental evidence about the delivery capacity *via* the different transdermal pathways can validate our CG models and should confirm the role of INF membranes for the specific formulation used in this work.

In summary, our results indicate an "onion peeling" mechanism of the nanodroplet for this particular cosmetic formulation, where the external layers are peeled off while the internal ones, which include the vitamins, tend to stay more intact. This process seems to be combined with another one, involving a component exchange mechanism of nanodroplet blend lipids with cholesterol from the INF bilayer. The resulting leaflet asymmetry and depletion of cholesterol in the INF membrane are both aspects that can lead to curvature and possibly trigger endocytosis. More importantly, both mechanisms indicate new possible strategies that could be used in rational *in silico* design of nanoemulsion formulations for transdermal delivery. For instance, in this particular system

studied here, one possible suggestion would be to fine-tune the saturation level of aliphatic chains of certain components as lecithins. As the preference for cholesterol in lipid systems seems to be related to the saturation level of aliphatic chains,[94] a higher ratio of hydrogenated lecithin could increase the partitioning of cholesterol from INF membranes to the nanodroplet. Additional future studies should also focus on the improvement of the simulation protocols, as the high-undulation in the membrane seems to promote membrane folding, given the periodic boundary conditions. The strong undulation hindered execution of simulations longer than 1 μs for INF membranes. In any case, we expect our work to open the way towards the Martini CG simulations of such delivery processes.

Conflicts of interest

There are no conflicts to declare.

Acknowledgements

The authors acknowledge financial support from the Brazilian agencies CNPQ, CAPES, FINEP, FAPESP and Boticário Group. Project FINEP 01.10.0661-00, FAPESP 2011/13250-0, FAPESP 2014/05975-2, CAPES 88887.068264/2014-00, CAPES 88881.062862/2014-01 and CNPQ 310375/2017-7. We thank the Center for Information Technology of the University of Groningen for providing access to the Peregrine high-performance computing cluster. We also acknowledge the computational services of Hipercubo cluster of Universidade do Vale do Paraíba. We would like to show our appreciation to Marcos Guilherme Machado, Herculano Martinho and Artur Cavaco-Paulo for relevant discussions and suggestions.

References

1 M. Jaiswal, R. Dudhe and P. K. Sharma, *3 Biotech.*, 2014, **5**, 123–127.
2 A. Gupta, H. B. Eral, T. A. Hatton and P. S. Doyle, *Soft Matter*, 2016, **12**, 2826–2841.
3 D. S. Shaker, R. A. Ishak, A. Ghoneim and M. A. Elhuoni, *Sci. Pharm.*, 2019, **87**, 17.
4 S. Baboota, F. Shakeel, A. Ahuja, J. Ali and S. Shafiq, *Acta Pharm.*, 2007, **57**, 315–332.
5 C. Qian, E. A. Decker, H. Xiao and D. J. McClements, *Food Chem.*, 2012, **135**, 1440–1447.
6 O. Sonneville-Aubrun, J.-T. Simonnet and F. L'Alloret, *Adv. Colloid Interface Sci.*, 2004, **108–109**, 145–149.
7 U. Sakulku, O. Nuchuchua, N. Uawongyart, S. Puttipipatkhachorn, A. Soottitantawat and U. Ruktanonchai, *Int. J. Pharm.*, 2009, **372**, 105–111.
8 S. Jain, V. Jain and S. C. Mahajan, *Adv. Pharm.*, 2014, **2014**, 1–12.
9 M. M. Fryd and T. G. Mason, *Annu. Rev. Phys. Chem.*, 2012, **63**, 493–518.
10 M. Rad-Malekshahi, K. M. Visscher, J. P. Rodrigues, R. De Vries, W. E. Hennink, M. Baldus, A. M. J. J. Bonvin, E. Mastrobattista and M. Weingarth, *J. Am. Chem. Soc.*, 2015, **137**, 7775–7784.
11 F. Bruxel, J. M. C. Vilela, M. S. Andrade, Â. Malachias, C. A. Perez, R. Magalhães-Paniago, M. C. Oliveira and H. F. Teixeira, *Colloids Surf., B*, 2013, **112**, 530–536.
12 J. K. Hensel, A. P. Carpenter, R. K. Ciszewski, B. K. Schabes, C. T. Kittredge, F. G. Moore and G. L. Richmond, *Proc. Natl. Acad. Sci. U. S. A.*, 2017, **114**, 13351–13356.
13 J. Thewalt and D. P. Tieleman, *J. Drug Targeting*, 2016, **24**, 768–773.
14 M. Ramezanpour, S. S. W. Leung, K. H. Delgado-Magnero, B. Y. M. Bashe, J. Thewalt and D. P. Tieleman, *Biochim. Biophys. Acta*, 2016, **1858**, 1688–1709.
15 M. B. A. Rahman, Q. Y. Huan, B. A. Tejo, M. Basri, A. B. Salleh and R. N. Z. A. Rahman, *Chem. Phys. Lett.*, 2009, **480**, 220–224.
16 R. A. Karjiban, M. Basri, M. B. A. Rahman and A. B. Salleh, *Int. J. Mol. Sci.*, 2012, **13**, 9572–9583.
17 S. Pirhadi and A. Amani, *Chem. Pap.*, 2020, **74**, 2443–2448.
18 S.-J. Lee, P. H. Schlesinger, S. A. Wickline, G. M. Lanza and N. A. Baker, *Soft Matter*, 2012, **8**, 7024.
19 S. Angioletti-Uberti, *npj Comput. Mater.*, 2017, **3**, 48.
20 H. M. Ding and Y. Q. Ma, *Nanoscale Horiz.*, 2018, **3**, 6–27.
21 G. Rossi, S. Salassi, F. Simonelli, A. Bartocci and L. Monticelli, *Biomembrane Simulations*, CRC Press, 2019, pp. 163–176.
22 X. Zhang, G. Ma and W. Wei, *NPG Asia Mater.*, 2021, **13**, 1–18.
23 H.-m. Ding and Y.-q. Ma, *Small*, 2015, **11**, 1055–1071.
24 C. Huang, Y. Zhang, H. Yuan, H. Gao and S. Zhang, *Nano Lett.*, 2013, **13**, 4546–4550.
25 T. Yue and X. Zhang, *ACS Nano*, 2012, **6**, 3196–3205.
26 R. Gupta, Y. Badhe, S. Mitragotri and B. Rai, *Nanoscale*, 2020, **12**, 6318–6333.
27 Z. Shen, H. Ye, X. Yi and Y. Li, *ACS Nano*, 2018, **13**, 215–228.
28 R. Vácha, F. J. Martinez-Veracoechea and D. Frenkel, *Nano Lett.*, 2011, **11**, 5391–5395.
29 Z. Shen, H. Ye, M. Kröger and Y. Li, *Nanoscale*, 2018, **10**, 4545–4560.
30 Z. Shen, H. Ye and Y. Li, *Phys. Chem. Chem. Phys.*, 2018, **20**, 16372–16385.
31 R. Gupta and B. Rai, *Nanoscale*, 2017, **9**, 4114–4127.
32 J. Wong-Ekkabut, S. Baoukina, W. Triampo, I.-M. Tang, D. P. Tieleman and L. Monticelli, *Nat. Nanotechnol.*, 2008, **3**, 363–368.
33 G. Rossi and L. Monticelli, *Biochim. Biophys. Acta, Biomembr.*, 2016, **1858**, 2380–2389.
34 Z. Shen, D. T. Loe, J. K. Awino, M. Kröger, J. L. Rouge and Y. Li, *Nanoscale*, 2016, **8**, 14821–14835.

35 R. Gupta and B. Rai, *Nanoscale*, 2018, **10**, 4940–4951.
36 R. Gupta and B. Rai, *Sci. Rep.*, 2017, **7**, 1–13.
37 S. Nangia and R. Sureshkumar, *Langmuir*, 2012, **28**, 17666–17671.
38 R. Guo, J. Mao and L.-T. Yan, *ACS Nano*, 2013, **7**, 10646–10653.
39 S.-J. Lee, P. H. Schlesinger, S. A. Wickline, G. M. Lanza and N. A. Baker, *Soft Matter*, 2012, **8**, 7024.
40 B. M. H. Bruininks, P. C. T. Souza and S. J. Marrink, *A Practical View of the Martini Force Field*, Springer New York, 2019, pp. 105–127.
41 B. M. H. Bruininks, P. C. T Souza, H. I. Ingólfsson and S. J. Marrink, *eLife*, 2020, **9**, e52012.
42 K. M. Gupta, S. Das and P. S. Chow, *Nanoscale*, 2021, **13**, 12916–12928.
43 E. M. Curtis, A. H. Bahrami, T. R. Weikl and C. K. Hall, *Nanoscale*, 2015, **7**, 14505–14514.
44 M. Lundborg, A. Narangifard, C. L. Wennberg, E. Lindahl, B. Daneholt and L. Norlén, *J. Struct. Biol.*, 2018, **203**, 149–161.
45 M. Lundborg, C. L. Wennberg, A. Narangifard, E. Lindahl and L. Norlén, *J. Controlled Release*, 2018, **283**, 269–279.
46 T. C. Moore, C. R. Iacovella, A. C. Leonhard, A. L. Bunge and C. McCabe, *Biochem. Biophys. Res. Commun.*, 2018, **498**, 313–318.
47 S. J. Marrink, H. J. Risselada, S. Yefimov, D. P. Tieleman and A. H. de Vries, *J. Phys. Chem. B*, 2007, **111**, 7812–7824.
48 T. A. Wassenaar, H. I. Ingólfsson, R. A. Böckmann, D. P. Tieleman and S. J. Marrink, *J. Chem. Theory Comput.*, 2015, **11**, 2144–2155.
49 C. D. Pizzol, personal communication, 2017.
50 J. A. Bouwstra and M. Ponec, *Biochim. Biophys. Acta, Biomembr.*, 2006, **1758**, 2080–2095.
51 J. Rogers, C. Harding, A. Mayo, J. Banks and A. Rawlings, *Arch. Dermatol. Res.*, 1996, **288**, 765–770.
52 G. Jenkins, *Mech. Ageing Dev.*, 2002, **123**, 801–810.
53 M. A. Lampe, A. L. Burlingame, J. Whitney, M. L. Williams, B. E. Brown, E. Roitman and P. M. Elias, *J. Lipid Res.*, 1983, **24**, 120–130.
54 N. Machado, L. dos Santos, B. Carvalho, P. Singh, C. T. Soto, N. Azoia, A. Cavaco-Paulo, A. Martin and P. Favero, *Comput. Biol. Med.*, 2016, **75**, 151–159.
55 H. I. Ingólfsson, M. N. Melo, F. J. van Eerden, C. Arnarez, C. A. Lopez, T. A. Wassenaar, X. Periole, A. H. de Vries, D. P. Tieleman and S. J. Marrink, *J. Am. Chem. Soc.*, 2014, **136**, 14554–14559.
56 I. Plasencia, L. Norlén and L. Bagatolli, *Biophys. J.*, 2007, **93**, 3142–3155.
57 J.-P. Hachem, D. Crumrine, J. Fluhr, B. E. Brown, K. R. Feingold and P. M. Elias, *J. Invest. Dermatol.*, 2003, **121**, 345–353.
58 S. J. Marrink, A. H. de Vries and A. E. Mark, *J. Phys. Chem. B*, 2004, **108**, 750–760.
59 G. Rossi, P. F. J. Fuchs, J. Barnoud and L. Monticelli, *J. Phys. Chem. B*, 2012, **116**, 14353–14362.
60 R. Alessandri, P. C. T. Souza, S. Thallmair, M. N. Melo, A. H. De Vries and S. J. Marrink, *J. Chem. Theory Comput.*, 2019, **15**, 5448–5460.
61 M. N. Melo, H. I. Ingólfsson and S. J. Marrink, *J. Chem. Phys.*, 2015, **143**, 243152.
62 P. C. T. Souza, R. Alessandri, J. Barnoud, S. Thallmair, I. Faustino, F. Grünewald, I. Patmanidis, H. Abdizadeh, B. M. H. Bruininks, T. A. Wassenaar, *et al.*, *Nat. Methods*, 2021, **18**, 382–388.
63 S. J. Marrink, V. Corradi, P. C. T. Souza, H. I. Ingólfsson, D. P. Tieleman and M. S. Sansom, *Chem. Rev.*, 2019, **119**, 6184–6226.
64 E. Lindahl, B. Hess and D. van der Spoel, *J. Mol. Model.*, 2001, **7**, 306–317.
65 H. Berendsen, D. van der Spoel and R. van Drunen, *Comput. Phys. Commun.*, 1995, **91**, 43–56.
66 D. V. D. Spoel, E. Lindahl, B. Hess, G. Groenhof, A. E. Mark and H. J. C. Berendsen, *J. Comput. Chem.*, 2005, **26**, 1701–1718.
67 B. Hess, C. Kutzner, D. van der Spoel and E. Lindahl, *J. Chem. Theory Comput.*, 2008, **4**, 435–447.
68 S. Pronk, S. Páll, R. Schulz, P. Larsson, P. Bjelkmar, R. Apostolov, M. R. Shirts, J. C. Smith, P. M. Kasson, D. van der Spoel, B. Hess and E. Lindahl, *Bioinformatics*, 2013, **29**, 845–854.
69 D. H. de Jong, S. Baoukina, H. I. Ingólfsson and S. J. Marrink, *Comput. Phys. Commun.*, 2016, **199**, 1–7.
70 R. Hockney, S. Goel and J. Eastwood, *J. Comput. Phys.*, 1974, **14**, 148–158.
71 L. Verlet, *Phys. Rev.*, 1967, **159**, 98–103.
72 G. Bussi, D. Donadio and M. Parrinello, *J. Chem. Phys.*, 2007, **126**, 014101.
73 H. J. C. Berendsen, J. P. M. Postma, W. F. van Gunsteren, A. DiNola and J. R. Haak, *J. Chem. Phys.*, 1984, **81**, 3684–3690.
74 M. Parrinello and A. Rahman, *J. Appl. Phys.*, 1981, **52**, 7182–7190.
75 N. Michaud-Agrawal, E. J. Denning, T. B. Woolf and O. Beckstein, *J. Comput. Chem.*, 2011, **32**, 2319–2327.
76 R. J. Gowers, M. Linke, J. Barnoud, T. J. E. Reddy, M. N. Melo, S. L. Seyler, J. Domański, D. L. Dotson, S. Buchoux, I. M. Kenney and O. Beckstein, *Proceedings of the 15th Python in Science Conference*, 2016, pp. 98–105.
77 C. R. Harris, K. J. Millman, S. J. van der Walt, R. Gommers, P. Virtanen, D. Cournapeau, E. Wieser, J. Taylor, S. Berg, N. J. Smith, *et al.*, *Nature*, 2020, **585**, 357–362.
78 V. Ramasubramani, B. D. Dice, E. S. Harper, M. P. Spellings, J. A. Anderson and S. C. Glotzer, *Comput. Phys. Commun.*, 2020, **254**, 107275.
79 J. D. Hunter, *Comput. Sci. Eng.*, 2007, **9**, 90–95.
80 P. Smith and C. D. Lorenz, 2021, bioRxiv.
81 S. Seo, M. Murata and W. Shinoda, *J. Phys. Chem. Lett.*, 2020, **11**, 5171–5176.
82 W. Humphrey, A. Dalke and K. Schulten, *J. Mol. Graphics*, 1996, **14**, 33–38.
83 C. Sheridan, *The Python Language Reference Manual*, Lulu Press, Inc, 2016.

84 J. D. Hunter, *Comput. Sci. Eng.*, 2007, **9**, 90–95.
85 M. A. Lampe, M. L. Williams and P. M. Elias, *J. Lipid Res.*, 1983, **24**, 131–140.
86 R. B. Gennis, *Biomembranes*, Springer New York, 1989.
87 V. Zoni, V. Nieto, L. J. Endter, H. J. Risselada, L. Monticelli and S. Vanni, *Front. Mol. Biosci.*, 2019, **6**, 124.
88 D. Bochicchio, E. Panizon, L. Monticelli and G. Rossi, *Sci. Rep.*, 2017, **7**, 1–9.
89 T. Hirama, S. M. Lu, J. G. Kay, M. Maekawa, M. M. Kozlov, S. Grinstein and G. D. Fairn, *Nat. Commun.*, 2017, **8**, 1–14.
90 T. Hirama and G. D. Fairn, *Commun. Integr. Biol.*, 2018, **11**, 1–4.
91 Y. Fan, Y. Zhang, W. Yokoyama and J. Yi, *Nanomaterials*, 2017, **7**, 349.
92 H. Schaefer and T. E. Redelmeier, *Skin Barrier: Principles of Percutaneous Absorption*, S Karger Ag, 1996.
93 A. Patzelt and J. Lademann, *Expert Opin. Drug Delivery*, 2020, **17**, 49–60.
94 O. Engberg, V. Hautala, T. Yasuda, H. Dehio, M. Murata, J. P. Slotte and T. K. Nyholm, *Biophys. J.*, 2016, **111**, 546–556.